4

IN SITU DIFFRACTION STUDIES OF SELECTED METAL–ORGANIC FRAMEWORK MATERIALS FOR GUEST CAPTURE/EXCHANGE APPLICATIONS

Winnie Wong-Ng

Materials Measurement Division, National Institute of Standards and Technology, Gaithersburg, MD

4.1 INTRODUCTION

4.1.1 Background

CO_2 is known to be the main anthropogenic contributor to the global climate change, and carbon mitigation approaches are critical for maintaining a sustainable future [1, 2]. At the current rates of energy consumption, known world coal reserves will last for more than 300 years, while known world natural gas reserves will last for about 60 years and oil reserves will last for about 40 years. Carbon capture/sequestration strategies are being developed for power plants worldwide which generally can be summarized in four steps: (1) CO_2 capture, (2) separation at point sources such as fossil-fueled power plants, followed by (3) transportation, and finally (4) long-term storage, primarily via deep underground injection [3].

Materials and Processes for CO_2 Capture, Conversion, and Sequestration, First Edition. Edited by Lan Li, Winnie Wong-Ng, Kevin Huang, and Lawrence P. Cook.

Capture is the key step for the capture/sequestration process, and is the most research-intensive. Gas retention in porous solids is technically and economically feasible; therefore, development of novel solid sorbent materials could provide a cost-effective way to capture CO_2.

Porous materials offer a wide range of compositions and structures that are suitable for adsorption and capture of CO_2 [4] and other guest molecules. These materials include zeolites [5, 6], activated carbon [7], smectites [8], oxide materials such as calcium oxide [9], lithium zirconates [10], and hydrotalcites [11]. There are also a vast number of reported metal–organic frameworks (MOFs) [12–40] that show diverse capture properties and applications at different pressures and temperatures. The field of MOF research has been rapidly expanding since the past decade. According to Zhou and Kitagawa [12], the surge of MOF research in recent years has been due to five factors: (1) advances in cluster chemistry, (2) maturation of organic synthesis (ligand design and post-synthetic modification of linkers), (3) improvements in evaluation of sorption and structural properties, (4) increase in interdisciplinary MOF investigations, and (5) an expanding potential for applications.

Various techniques have been applied for characterization of MOFs and the associated guest molecules, including structural techniques, adsorption techniques, spectroscopic techniques, and modeling techniques. Up to the present, considerable knowledge of MOF structure and properties has been accumulated; however, there is still a lack of detail concerning guest adsorption mechanisms and guest–host interactions, which are necessary for designing more efficient sorptive materials.

4.1.2 *In Situ* Diffraction Characterization

Instrumental designs [41–46] for *in situ* diffraction experiments concerning adsorption of guest molecules in the cavities of MOFs and the synthesis and monitoring MOF phase formation have attracted increasing attention in recent years [32, 47–76]. These experiments continue to facilitate our understanding of adsorption/desorption properties and detailed adsorption mechanisms of various guest species. In particular, neutron and X-ray synchrotron-based diffraction have been used successfully to identify CO_2 adsorption sites in MOFs.

Time-resolved, *in situ* single-crystal X-ray diffraction and powder diffraction techniques provide the opportunity to study crystalline nanoporous materials under realistic ambient and non-ambient conditions. These measurements will provide experimental data to compliment data that are obtained theoretically or by spectroscopic methods. *In situ* single-crystal and powder diffraction techniques are being utilized in national laboratory facilities worldwide. As these special facilities have limited availability and large expenses associated with their usage, a summary of the applicability of laboratory powder X-ray diffraction to study the location of CO_2 in solid sorbents is also included here.

Example of applications of *in situ* diffraction experiments include detection of unstable intermediate stage during guest exchange [41]; materials screening for post-combustion CO_2 capture [45]; phase transformation (reversible phase transformation [47]; guest-induced structural transition [48, 49], and multiple-phase transition upon selective adsorption [57, 66]); dynamic CO_2 sorption behavior [50]; identification of adsorption/binding site of CO_2 and other gases [51, 67]; breathing modes of flexible MOF [52–56]; monitor of mechanochemical reaction-metastable intermediate [58]; gas adsorption mechanism [59]; capture of metastable intermediates in during the MOF formation [60]; internal pore location of CO_2 [62]; *in situ* synthesis and phase formation of MOFs [61, 63, 65, 70–72]; dynamic gas adsorption sites [64]; guest–host intermolecular interactions [68]; topological change/framework distortion related to solvent exchange [69]; kinetics of liquid-enhanced gas uptake [73]; high speed of transient molecular adsorption [74]; and crystal engineering of large discrete cavities [75].

The two goals of this chapter are (1) to give a brief summary of *in situ* studies of MOFs with regard to sorption of guests (i.e., H_2O, CO_2), for single crystals as well as powder samples, and (2) to illustrate examples emphasizing the importance of *in situ* techniques, particularly for unraveling the processes related to the complex behavior of MOF materials.

4.2 APPARATUS FOR *IN SITU* DIFFRACTION STUDIES

Since 2005, there have been a number of papers discussing *in situ* studies of porous materials for capture of gases and liquids [41–46]. We will briefly describe several representative cell- and chamber-based designs.

4.2.1 Single-Crystal Diffraction Applications

4.2.1.1 Environmental Control Cell For *in situ* single-crystal diffraction studies, it is important to have appropriate goniometers that house the single crystals and allow the presence of gas in either a closed system or an open system where the gas is allowed to flow through. Recently, an environmental control cell (ECC) has been incorporated as part of a single-crystal goniometer head [41]. This ECC can be used with any commercially available single-crystal X-ray instrument that is equipped with a flexible tubing source capable of delivering static or dynamic vacuum, liquids, or gases.

Figure 4.1 gives the description of the device and the image of the assembled ECC mounted on a standard goniometer head [41]. The base of the device is modeled after a standard magnetic base and is held by a setscrew. The components of this simple setup include a bent needle, the ECC body, a capillary retaining screw, an o-ring, a capillary, a setscrew, and a thin glass fiber for sample mounting. The cell is easy to use and is completely reusable. The device is nearly identical in size to standard single-crystal mounts, so a full unrestricted range of motion is expected for most commercial goniometers.

Figure 4.1 Image of the assembled ECC mounted on a standard goniometer head (*left*), with exploded view of ECC components at *right*: a, bent 18 gauge tube; b, ECC body; c, capillary retaining screw; d, o-ring; e, capillary (shortened and sealed with glue); f, set-screw; g, sample mounted on thin glass fiber. *Source*: Cox et al. 2015 [41]. Reproduced with permission of the International Union of Crystallography, http://journals.iucr.org/

4.2.1.2 Environmental Gas Cell Another environmental gas cell (EGC) which also allows a single crystal to be placed either under vacuum or exposed to a pure gas or a gas mixture was designed by Warren et al. [42] (Figure 4.2). The cell utilizes the Hampton Research short XYZ goniometer head[1] with no modification to allow space for the gas/vacuum pipe connection. The cell body is made of borosilicate or quartz capillary tubing. The capillary tube is glued into a small recess of the EGC head. The EGC base and head were fabricated from stainless steel. A simple Swagelok stainless steel two-way valve was connected to the EGC Nalgene tube allowing vacuum or gas to be fed to the EGC head. Details are given in References [42] and [43].

4.2.1.3 Quartz Pressure Cell A simple and inexpensive pressure cell for single-crystal study at pressures up to 1 kbar and a special attachment for mounting the cell onto a goniometer were designed by Yufit and Howard [44]. Based on a number of different previous versions, their improved design is much more convenient to use. It also takes advantage of modern diffractometer capabilities, including the use of area detectors.

[1] Certain trade names and company products are mentioned in the text or identified in illustrations in order to specify adequately the experimental procedure and equipment used. In no case does such identification imply recommendation or endorsement by National Institute of Standards and Technology, nor does it imply that the products are necessarily the best available for the purpose.

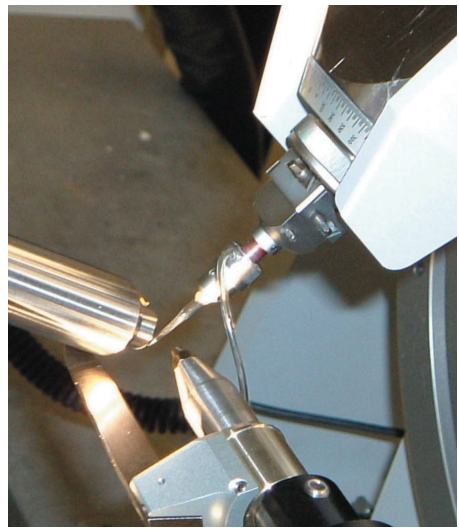

Figure 4.2 Prototype environmental gas cell (EGC) (SRS on Station 9.8). *Source*: Adapted from Warren et al. 2009 [42] and Cernik et al. 1997 [43].

A schematic of the **quartz pressure cell** (QPC) is shown in Figure 4.3a, where the basic components are illustrated. Figure 4.3b illustrates a QPC on the geometer of the Bruker Smart CCD 6000 diffractometer. Monitoring the pressure was performed using a standard pressure gauge attached to the pressure line.

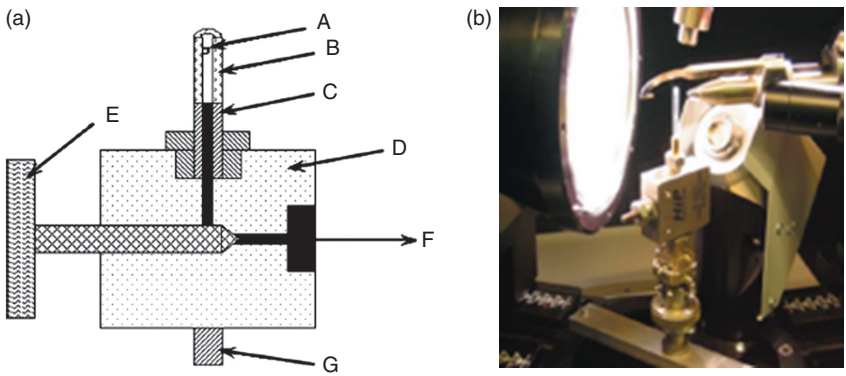

Figure 4.3 (a) Schematic of the QPC. A, crystal; B, quartz capillary; C, brass part of quartz-metal seal; D, valve 30-12HF2; E, removable handle; F, standard 1/8″ connector to a pressure line; G, stud for attachment of the QPC to the goniometer head. (b) QPC on the goniometer of the Bruker Smart CCD 6000. *Source*: Yufit and Howard 2005 [44]. Reproduced with permission of the International Union of Crystallography, http://journals.iucr.org/

4.2.2 Powder Diffraction Applications

4.2.2.1 Environmental Chambers Different options for environmental chambers are provided by manufacturers such as Panalytical, Bruker, and Rikagu Inc. There are also various custom-built chambers such as those being used at national beamlines. Figure 4.4 illustrates several non-ambient chambers (Anton Paar Instruments, Inc.) used by diffractometer manufacturers. The XRK900 chamber can be used with gases such as CO_2 up to 10 bars (300–1175 K). The TTK450 chamber operates from 80 to 723 K, whereas the HTK16 chamber operates from 300 to 1875 K.

4.2.2.2 Simultaneous PXRD and DSC Techniques The XRD-DSC system that was developed by Woerner et al. [45] is composed of a Rigaku Ultima IV diffractometer (CuKα radiation with a D/TeX high-speed linear position sensitive detector), a Rigaku XRD-DSC stage, Rigaku HUM-1 humidity generator, ULVAC vacuum pump (6.66×10^{-5} kPa), a vacuum manifold, and a custom-built humid atmosphere swing chamber (Figure 4.5). The humid atmosphere swing chamber (HASC) was necessary to buffer between the humidity generator and a XRD-DSC stage so that both humid atmosphere and vacuum swings could be performed. The design of the XRD-DSC system allows for three types of sample treatments, namely, *in situ* activation, vacuum swing, and atmosphere swing.

4.2.2.3 Oxford-Diamond* In Situ *Cell Oxford-Diamond *In Situ* Cell (ODISC) [46] is a versatile, infrared-heated, chemical reaction cell developed by Moorhouse for *in situ* study of a range of chemical syntheses using time-resolved, energy-dispersive X-ray diffraction (EDXRD) on beamline I12 at the Diamond Light Source. A specialized reactor configuration has been constructed to enable *in situ* EDXRD investigation of samples under non-ambient conditions. One can use various sample vessels such as alumina crucibles, steel hydrothermal autoclaves, and

Figure 4.4 Non-ambient chambers for *in situ* X-ray diffraction studies. *Source*: Courtesy of Anton Paar Instruments, Inc.

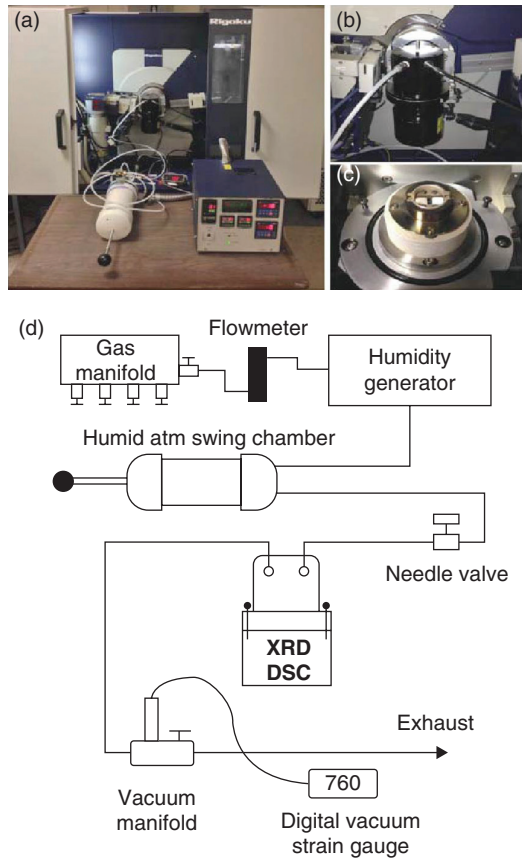

Figure 4.5 (a) Photo of a complete XRD-DSC system, (b) XRD-DSC stage with sealing cap, (c) XRD-DSC attachment without cap showing the Al_2O_3 standard and sample powder on aluminum pans, and (d) schematic of the entire XRD-DSC system. *Source*: Woerner et al. 2015 [45]. Reproduced with permission of American Chemical Society.

glassy carbon tubes, at temperature up to 1200°C. Figure 4.6a gives the schematic of the ODISC furnace and Figure 4.6b shows the cross section of the lower section of the cell.

4.3 *IN SITU* SINGLE-CRYSTAL DIFFRACTION STUDIES OF MOFs

In situ diffraction studies as applied to porous MOF materials are illustrated with the following 12 examples, which include neutron, synchrotron, and conventional laboratory X-ray diffraction under ambient and non-ambient conditions. Crystallographic

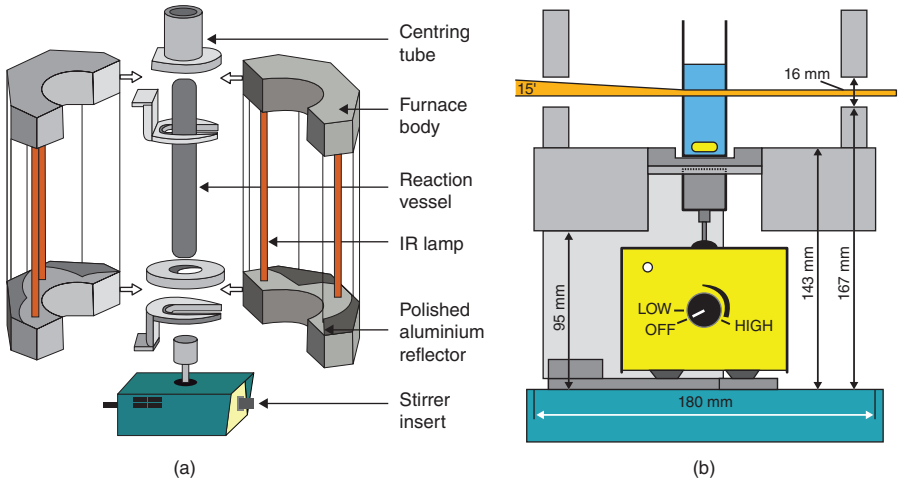

Figure 4.6 (a) Schematic of the ODISC furnace. (b) Cross-sectional diagram of the lower section of the ODISC cell. *Source*: Moorhouse et al. 2012 [46]. Reproduced with permission of American Institute of Physics.

observation of adsorbed gas molecules at high temperatures is a highly challenging task due to their rapid motion. In the selected examples, the following features are emphasized: crystal-to-crystal phase transformation, structure transformation due to the presence of guests, phase transformation induced by changes of guests (CO_2/N_2), intermediate stage of guest exchange, mechanism of CO_2 adsorption, breathing mode of flexible MOFs, multiphase-transition upon selective CO_2 adsorption, *in situ* metastable intermediate transformation, location of CO_2 in the pores of MOFs, reversible gas sorption, *in situ* study of framework formation, and fast screening of sorbents for CO_2 capture using combined *in situ* XRD and DSC.

4.3.1 Thermally Induced Reversible Single Crystal-to-Single Crystal Transformation

Allan et al. [47] demonstrated the detailed reversible phase transformation of single-crystal $Cu_2(OH)(C_8H_3O_7S)(H_2O)\cdot 2H_2O$ (Cu-SIP-3) due to the presence/absence of water using *in situ* X-ray diffraction as a function of temperature. X-ray diffraction data were collected over a range of 150–500 K at the Advanced Light Source, Lawrence Berkeley National Laboratory. *In situ* loading experiments were performed using the EGC goniometer head designed by Warren et al. [42].

Cu-SIP-3 undergoes a phase transformation on dehydration. As a result of the loss of coordinated water, there is a change in metal coordination which involves the breaking of several bonds in the low-temperature structure. At temperatures below a dehydration-induced phase transition ($T < 370$ K) the structure was confirmed as being hydrated (left drawings of Figures 4.7a and 4.7b). In the

temperature range where the transition takes place (370 K < T < 405 K), no discrete, sharp Bragg peaks were found in the X-ray diffraction patterns, indicating a significant loss of long-range order. At T > 405 K, the Bragg peaks return and the structure corresponds to a dehydrated phase, Cu-SIP-3 (right drawings of Figures 4.7a and 4.7b). At a temperature up to 150 K, the structure of hydrated $Cu_2O_{11}C_8S$ is monoclinic $P2_1/n$ (a = 7.2949(4), b = 18.2726(6), c = 10.1245(6), β = 139.172(4)°). At 500 K, the sample becomes dehydrated $Cu_4O_{16}C_{16}S_2$ (Cu-SIP-3). While the dehydrated form is also monoclinic $P2_1/n$, the cell parameters are different: a = 13.792(2) Å, b = 19.430(4) Å, c = 12.057(2) Å, β = 139.172(4)°. After the crystal was exposed to moisture at 293 K, the structure of the rehydrated sample ($Cu_2O_{11}C_8S$) returns to monoclinic $P2_1/n$ (a = 7.3333(14) Å, b = 18.153(3) Å, c = 10.1729(19) Å, β = 94.379(4)°). Therefore, one can conclude unambiguously using *in situ* X-ray experiment that the loss of coordinated guest water molecules necessitates coordination changes, leading to lowering of symmetry and almost doubling the size of the asymmetric unit.

4.3.2 Structure Transformation Induced by Presence of Guests

Takamizawa et al. [48] used combined single-crystal and *in situ* powder X-ray to study crystal transformation from an empty host $Rh_2(bza)_4(pzy)$ (where bza = benzoate and pzy = pyrazine) to the material after CO_2 molecules were adsorbed. The structure of $Rh_2(bza)_4(pzy)$ consists of parallel one-dimensional chains and isolated cavities of 9 × 4 × 3 Å with narrow gaps of approximately 1 Å at the four corners of the cavities (Figure 4.8). The crystal structure of the host crystal without CO_2 and with saturated (sealed-in) CO_2 is rather different, namely, triclinic P-1 versus monoclinic ($C2/c$ at 90 K and $C2/m$ at 298 K), respectively [35]. The structure transformation was a result of the changing of interchain distances, slipping of neighboring chains, and tilting of the π–π stacked phenyl rings of the (bza) ligand

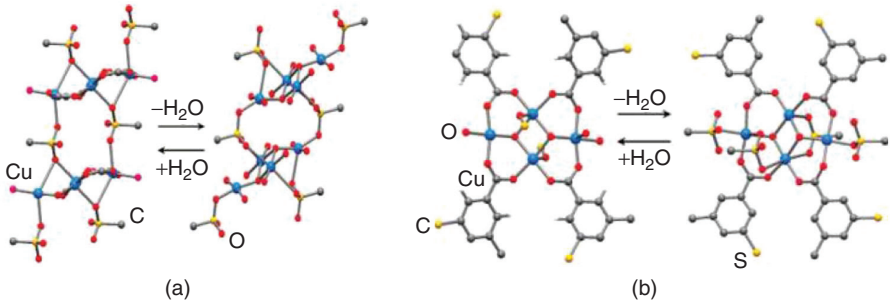

Figure 4.7 (a) Chains of copper tetramers in the low-temperature (*left*) and high-temperature (*right*) structures of Cu-SIP-3. (b) Copper tetramers in the low-temperature (*left*) and high-temperature (*right*) structures (Color scheme: blue balls-Cu, red balls-O, yellow balls-S, and gray balls-C). *Source*: Allan et al. 2010 [47]. Reproduced with permission of American Chemical Society.

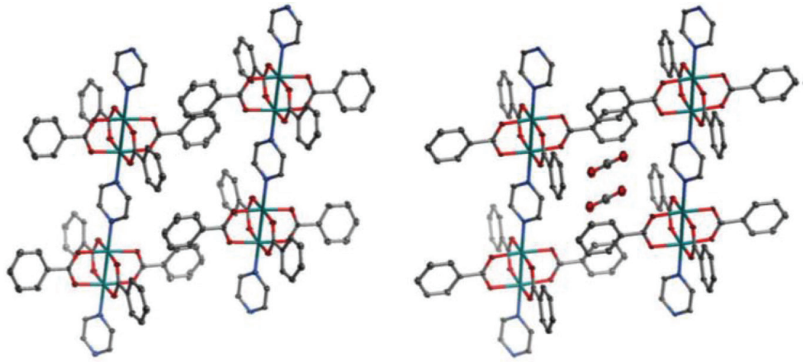

Figure 4.8 The single-crystal structures of (a) $[Rh_2(bza)_4(pyz)]$ and (b) CO_2-included $[Rh_2(bza)_4(pyz)]$ measured at 90 K. Thermal ellipsoids are drawn at 30% probability. *Source*: (a) Zhang et al. 2014 [35]. Reproduced with permission of Royal Society of Chemistry. (b) Takamizawa et al. 2010 [48]. Reproduced with permission of American Chemical Society.

(i.e., tilting of the benzene ring about 9° away from the chain). Figure 4.8b shows that the adsorbed CO_2 molecules were confined in the channel and interact with the phenyl rings via phenyl and CO_2-quadrupole interaction. *In situ* high-temperature XRD showed the amount of uptake of adsorbed CO_2 decreases as the temperatures increase. Evidence for the diffusion of gas into the crystal through the narrow gaps was obtained from sorption measurements. Interestingly, variable-temperature ^2H NMR spectroscopy in a constant CO_2 pressure (0.1 MPa) showed that the "rotating door" motions of the flipping benzene rings of the host skeleton were responsible for CO_2 diffusion between cavities (Figure 4.9) [49].

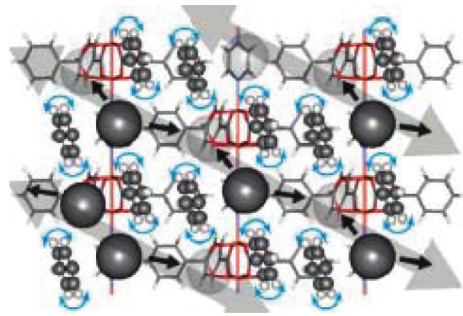

Figure 4.9 Schematic diagram of the "rotating door" motion of the flipping benzene rings of the host skeleton consisting of inner channel walls in $[Rh_2(bza)_4(pyz)]$. The light gray arrow indicates the channel direction where CO_2 diffuses. *Source*: Takamizawa et al. 2010 [49]. Reproduced with permission of American Chemical Society.

4.3.3 Dynamic CO_2 Adsorption Behavior

Using a bis-triazolate ligand and tetrahedral Zn(II) ion, Liao et al. [35, 50] synthesized a flexible porous coordination polymer $[Zn_2(btm)_2].4H_2O$, H_2btm = (bis(5-methyl-1H-1,2,4-triazol-3-y1) methane) ((MAF-23·$4H_2O$). This porous polymer is functionalized with pairs of uncoordinated triazolate N-donors that can be used as guest-chelating sites to give CO_2/N_2 selectivity. The dynamic CO_2 sorption behavior was monitored by single-crystal X-ray diffraction. According to Zhang et al. [35], MAF-23 showed high saturation CO_2 uptake ($3CO_2$ per formula unit). Single-crystal structures of MAF-23·xCO_2 (x = 0.00, 0.07, 1.5, and 2.8) were measured at 195 K. In MAF-23·$0.07CO_2$, a CO_2 molecule was chelated by one of the two crystallographic independent chelating claws, which possessed a methyl group at the *ortho*-position of the N-donor, demonstrating the weak electron donating effect of the methyl group (Figure 4.10). When the CO_2 uptake increases, the unit cell volume of the MAF-23 continuously increases due to the distortion of coordination geometries of the Zn(II) ions and ligand shapes around the methylene groups. As CO_2 increases, there is a strong binding affinity due to the action of the guest-chelating claws. The cage continues to deform and there is a balance between attraction of N-donor with the CO_2 molecule and the repulsion between the CO_2 molecules. With x = 1–4, MAF-23·xCO_2 crystallizes in monoclinic $P2_1/n$. At 195 K, MAF-23·xCO_2 showed a Type I CO_2 sorption isotherm without hysteresis (Figure 4.11), giving an apparent Langmuir surface area of 622(5) $m^2\ g^{-1}$ and a pore volume of 0.21 $cm^3\ g^{-1}$.

4.3.4 Unstable Intermediate Stage During Guest Exchange

A successful trapping of a metastable intermediate hydrate phase was illustrated by Cox et al. using the ECC with a previously reported MOF [Co(5-NH_2-bdc)

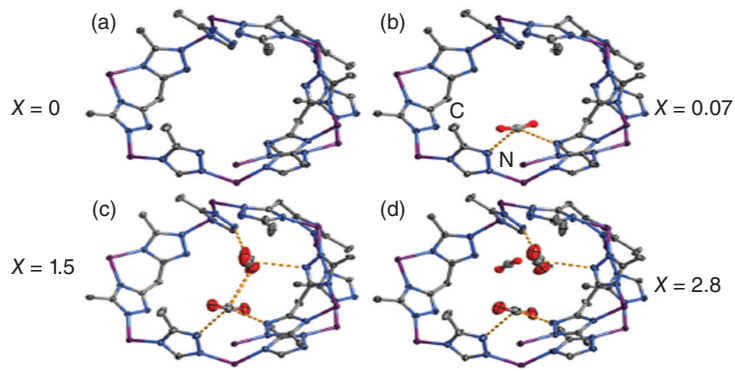

Figure 4.10 Single-crystal structures of MAF-23•xCO_2 measured at 195 K (a–d). x = 0.00, 0.07, 1.5, and 2.8, respectively. Hydrogen atoms are omitted for clarity. Short intermolecular contacts are shown as dashed bonds. *Source*: Liao et al. 2012 [50]. Reproduced with permission of American Chemical Society.

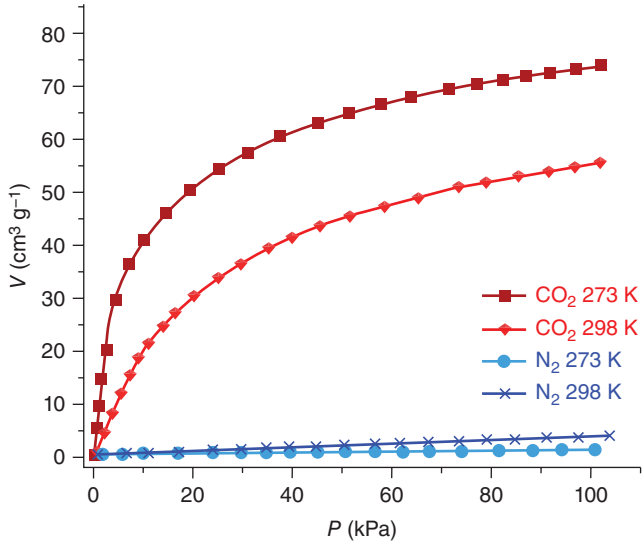

Figure 4.11 CO_2 and N_2 adsorption (solid) and desorption (open) isotherms of MAF-23•*x*CO_2. *Source*: Liao et al. 2012 [50]. Reproduced with permission of American Chemical Society.

$(bpy)_{0.5}(H_2O)]\cdot 2H_2O$ (5-NH_2-bdc = 5-aminoisophthalate, bpy = 4,4′-bipyridine) [41]. *In situ* single-crystal X-ray diffraction experiments performed under dynamic gas flow conditions revealed this highly flexible framework is capable of exchanging a wide variety of guest molecules in a single-crystal-to-single crystal manner. It was reported that the anhydrous framework [Co(5-NH_2-bdc)$(bpy)_{0.5}$] was prepared by heating the trihydrate phase under a vacuum at 393 K for 2 h. As the crystal structures contain multiple crystallographically unique solvent molecules, Cox et al. were interested to see if guest exchange, in particular the dehydration reaction of the crystal, occurred via the formation of discrete structures possessing an intermediate number of solvent molecules.

The initial trihydrate structure (Figure 4.12b) has one water molecule coordinated to the Co metal center and two "free" water molecules held within the pore by hydrogen bonds. The second structure, obtained after 15 min of nitrogen flow, is that of a previously unreported dihydrate phase [Co(5-NH_2-bdc)$(bpy)_{0.5}(H_2O)]\cdot 2H_2O$. When the flow of dry nitrogen gas is halted, the dehydrate phase (Figure 4.12a) is converted back to the starting trihydrate phase within 5 min, presumably by reabsorbing moisture from the air. Sealing the capillary effectively halts the rehydration back reaction and thereby enables the collection of diffraction data on the metastable dihydrate phase. In summary, the ECC was capable of stabilizing a novel metastable intermediate in the dehydration reaction.

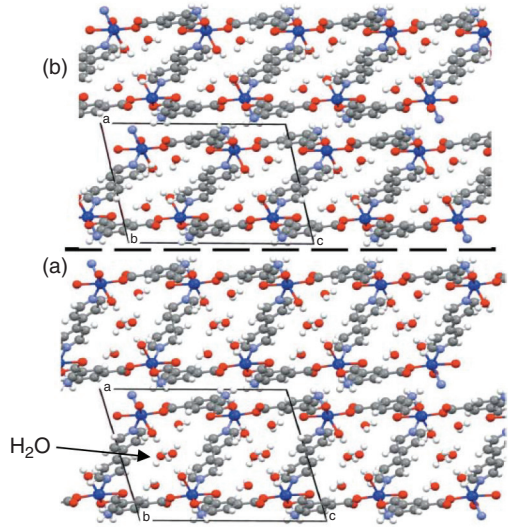

Figure 4.12 The reversible conversion of a trihydrate (a), single-crystal structure to dehydrate (b), is conducted by flowing dry N_2 through the crystal, and then by halting the flow. The appearance and disappearance of the water molecule can be seen. *Source*: Cox et al. 2015 [41]. Reproduced with permission of the International Union of Crystallography, http://journals.iucr.org/

4.3.5 Mechanism of CO_2 Adsorption

Miller et al. [51] studied the adsorption mechanism of the microporous scandium terephthalate, $Sc_2(O_2CC_6H_4CO_2)_3$ (ScBDC), an attractive small-pore model sorbent for small molecules relevant to CO_2 separation technologies. The mechanism of adsorption of CO_2 has been determined by single-crystal synchrotron X-ray diffraction at ≈230 K at the European Synchrotron Radiation Facility, Grenoble, France. A custom-made gas delivery system was used for the *in situ* gas pressure studied from 1 to 9 bar of CO_2.

The details of the adsorption mechanisms were obtained with *in situ* studies from p_{CO_2} = (0–1) bar. At p_{CO_2} = 1 bar, the symmetry of the crystal has changed from orthorhombic *Fddd* to monoclinic *C*2/*c* through tilts in the terephthalate linkers with the presence of CO_2. CO_2 molecules take up different sites in two symmetrically different channels that result from the symmetry change. Figure 4.13a depicts the ScO_6 octahedra, and three different terephthalate groups, namely, group 1, group 2a, and group 2b. Group 1 in channel A was found having the orthorhombic structure. Groups 2a and 2b were a result of the rotations of the terephthalate groups. In channel A, the occupancy of CO_2 is close to one and the CO_2 molecule axis is aligned so that the O atom is pointed toward the hydrogen atoms of the framework phenyl group. In channel B, there are two symmetry-related sites for CO_2 but they

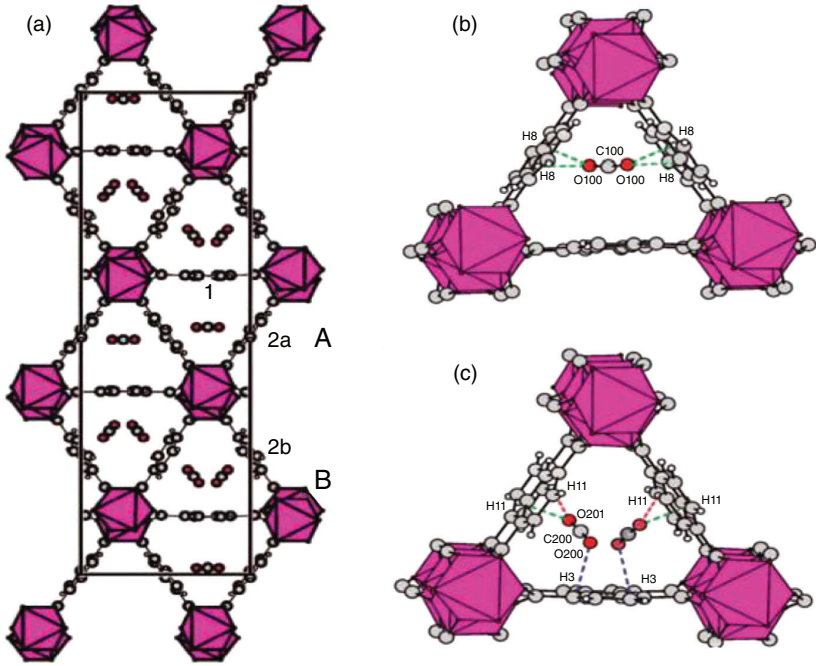

Figure 4.13 (a) Slices of CO_2 molecules adsorbed in ScBDC at 1 bar and 235 K, viewed down the channel axes. In rows of channel types A and B, the channels are no longer identical due to different rotation of the terephthalate groups labeled as types 2a and 2b. The environments of CO_2 in the triangular pores in channels of types A and B are illustrated further in (b) and (c), respectively. *Source*: Miller et al. 2009 [51]. Reproduced with permission of American Chemical Society.

cannot be simultaneously occupied. The environments of CO_2 in the triangular pores in channel types A and B are shown more clearly in Figures 4.13b and 4.13c.

4.4 POWDER DIFFRACTION STUDIES OF MOFs

4.4.1 Synchrotron/Neutron Diffraction Studies

The breathing behavior of MOFs for gas adsorption has been reviewed by Alhamami et al. [52]. The unique breathing behavior upon adsorption of gases or solvents underlies their potential application as host materials in gas storage for renewable energy. This unique behavior has attracted widespread attention to designing, understanding, and utilizing properties of these materials. The tools of investigation, in addition to the use of *in situ* diffraction, also include calorimetry, nuclear magnetic resonance (NMR), Fourier transform infrared spectroscopy, and theoretical modeling.

4.4.1.1 Breathing Modes of Flexible MOFs A unique feature, which distinguishes some MOFs from conventional porous materials, is the ability to "breathe," that is, to expand or contract in response to external stimuli such as variation in temperature. Such flexible networks are sometimes referred to as "breathing" MOFs. The best-known materials exhibiting breathing mode characteristics comprise the MIL-53 series [52–56]. Structurally, these materials are formed by connections of corner-sharing $MO_4(OH)_2$ octahedra linked by 1,4-benzenecidarboxylic (BDC) acids. As the MIL53 (Al, Cr) materials are synthesized hydrothermally (MIL-53as), the channels are filled with disordered BDC and H_2O molecules (narrow pore (np) structures) [53]. The narrow pore structure is formed by hydrogen bonding between the water molecule and the carboxylic and hydroxyl groups of the host molecules. Upon dehydration at high temperature, the MIL-53 gives rise to a large pore (lp) structure due to the absence of interactions. Therefore, using heat as an external stimulus, a reversible conversion between the hydrated MIL-53 (np) and the dehydrated MIL-53 form (lp) is observed (Figure 4.14a).

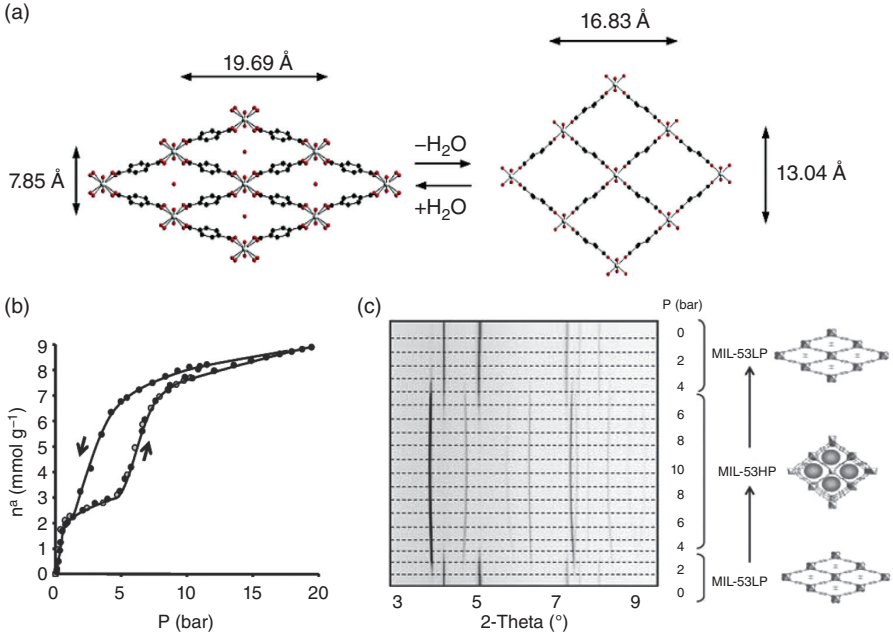

Figure 4.14 (a) Schematic representation of the reversible hydration–dehydration of MIL-53np and MIL-53lp. *Source*: Seere et al. 2002 [53]. Reproduced with permission of American Chemical Society. (b) Adsorption isotherms of MIL-53 (Cr) showing hysteresis loop. (c) Powder XRD patterns of MIL-53 (Cr) under various pressures of CO_2 at 293 K. *Source*: Seere et al. 2007 [54]. Reproduced with permission of John Wiley & Sons.

An interesting adsorption behavior that has been observed in MIL-53 (Cr) is the adsorption of a large amount of CO_2 molecules at room temperature [54] (Figure 4.14b). After a fast uptake at low pressure (approximately 2–3 mmol g^{-1}), the isotherm reaches its first plateau between 1 and 4 bar followed by an adsorption of more than a double amount of CO_2 at higher pressures. The desorption branch returns to coincide with the adsorption branch at approximately 2 bar. This unusual result could be interpreted as follows: while the degassed solid exhibits an expected lp structure, the first small portion of CO_2 would force the pore to be np due to host–guest interaction. A further absorption of CO_2 at higher pressure reopens the pore to accept more CO_2. This interpretation agrees with *in situ* diffraction experiments performed at synchrotron radiation facilities under 1–10 bar CO_2 (Figure 4.14c).

4.4.1.2 Multiple-Phase Transitions upon Selective CO_2 Adsorption

Another interesting system (provided by Henke et al. [57]) that exhibits multiple-phase transition and remarkable breathing behavior with respect to the presence/absence of polar molecules in the pores is the flexible alkyl ether-functionalized MOF $[Zn_2(BME\text{-}bdc)_2(dabco)]_n$, (BME-bdc = 2,5-bis(2-methoxyethoxy)-1,4-benzenedicarboxylate, dabco = 1,4-diazabicyclo[2.2.2]octane) [57]. Apparently, the dried sample exhibits a narrow pore form with almost no accessible porosity. Upon adsorption of polar guest molecules (DMF, EtOH), the framework transforms to an open pore form, with accompanying increase of unit cell volume. This flexibility (contraction of network) is because of the strong interaction between the 2-methoxyethoxy substituents, when guest molecules are absent. This situation is opposite to the situation of MIL-53 discussed previously. When guest molecules are present in this case (CO_2), the unit cell volume increases. Due to the slow adsorption kinetics, an unexpected metastable intermediate form could be identified.

Figure 4.15 gives a sorption isotherm of $[Zn_2(BME\text{-}bdc)_2(dabco)]_n$ at 195 K. The feature of this isotherm includes a stepwise adsorption and a large hysteresis, typical for flexible MOFs that undergo a structural transition upon adsorption of guest molecules. The quadrupole moment of CO_2 enables the gas to penetrate into the pore because of weak intermolecular interactions. It stays at the narrow pore region from $p_{CO_2} = 0$ to 200 mbar. The steep uptake at 200 mbar signifies a structural transformation from the narrow pore to the open pore form. On the desorption branch a large hysteresis was observed which was due to the "breathing" framework.

The *in situ* XRD patterns corroborate the transformation explanation. Figure 4.16 shows a close-up view of the low angle region of the X-ray patterns recorded as a function of partial pressure of CO_2. The lowest angle peak reflection (2.73° – (001)) is in roughly the same position for all three phases. Structural models of the three different states of $[Zn_2(BME\text{-}bdc)_2(dabco)]_n$ upon CO_2 adsorption at 195 K are shown in Figure 4.17. The cell parameters are all rather similar to each other in the three forms. Up to 300 mbar, only "narrow pore form" is present. The unit cell is slightly expanded at 200 mbar and shrinks at 300 mbar. From 400 to 900 mbar, an intermediate pore form appears which has a mixture of the narrow, intermediate, and open pore form. At 1000 mbar, the "open pore form" almost exclusively exists.

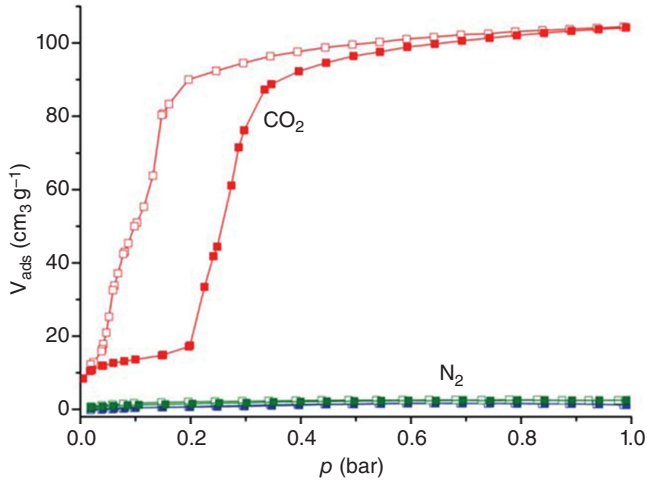

Figure 4.15 Sorption isotherms at 195 K. Adsorption and desorption branches are shown with closed and open symbols. *Source*: Henke et al. 2011 [57]. Reproduced with permission of Royal Society of Chemistry.

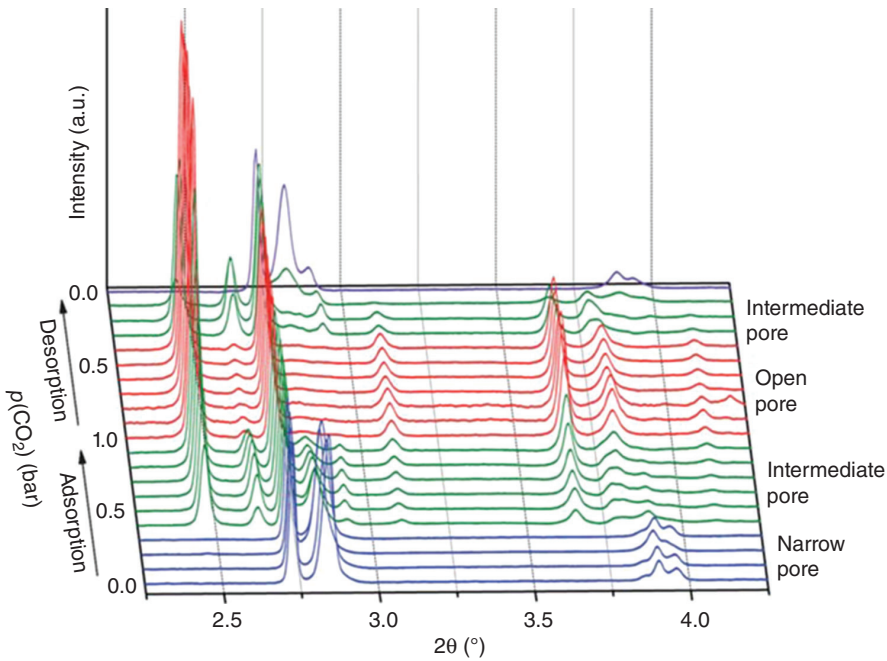

Figure 4.16 Lower angle region of the PXRD patterns recorded at variable CO_2 pressure (λ = 0.4592 Å). Patterns representing the narrow pore (blue), open pore (red) and intermediate pore form (green). *Source*: Henke et al. 2011 [57]. Reproduced with permission of Royal Society of Chemistry.

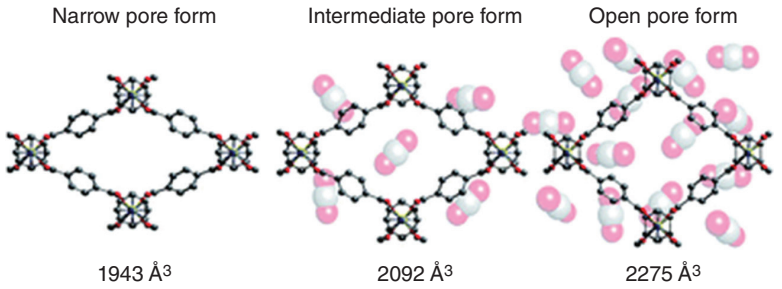

Figure 4.17 Structural models of the three different states of $[Zn_2(BME\text{-}bdc)_2(dabco)]_n$ upon CO_2 adsorption at 195 K as a function of increasing p_{CO_2} (L → R from 0 to 1000 mbar). Disordered 2-methoxyethoxy substituents and hydrogen atoms are not included in the model structures. *Source*: Henke et al. 2011 [57]. Reproduced with permission of Royal Society of Chemistry.

4.4.1.3 Metastable Intermediate Transformation Katsenis et al. [58] used *in situ*, real-time synchrotron powder X-ray diffraction to capture and to monitor a metastable, novel-topology intermediate of a mechanochemical transformation. While amorphization on milling is a well-known phenomenon, spontaneous recrystallization of the amorphous phase by continued milling has not been described prior to the cited work. During the synthesis of MOF Bis (2-methylimidazolyl)-zinc (also known as ZIF-8) by applying the grinding technique, they observed the unexpected amorphization. On further milling, recrystallization into a non-porous material via a metastable intermediate new phase, katsenite (kat), took place. The sequence of solid-state transformations in the reaction of ZnO and 2-methylimidazole (HMeLm) is shown in Figure 4.18. The new topology provides evidence that milling transformation can involve short-lived, structurally

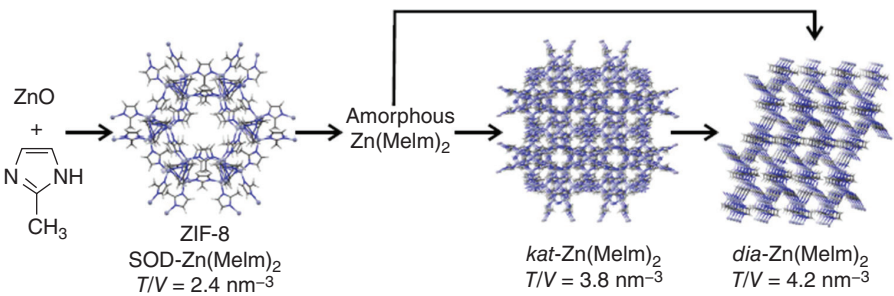

Figure 4.18 Sequence of solid-state transformations in the reaction of ZnO and sodalite (SOD) framework, ZIF-8. *Source*: Katsenis et al. 2015 [58]. Reproduced with permission of Nature Publishing Group.

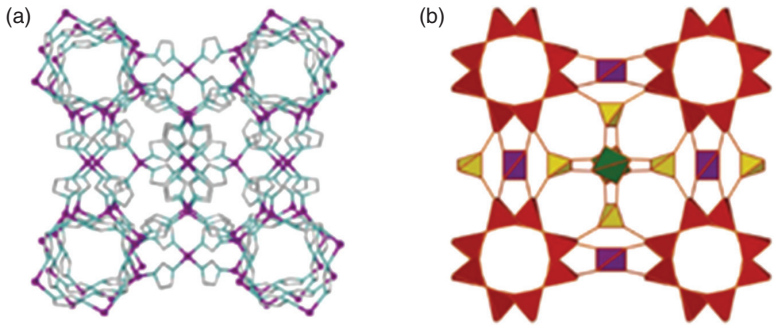

Figure 4.19 Structure of kat-Zn(MeIm)2 viewed along the crystallographic *c* direction: (a) ball-and-stick representation and (b) the kat framework with different coloring for each type of vertex, represented by its vertex figure. *Source*: Katsenis et al. 2015 [58]. Reproduced with permission of Nature Publishing Group.

unusual phases. Structure of kat-Zn(Melm)$_2$ is shown in Figures 4.19a and 4.19b. kat-Zn(Melm)$_2$ contains pores consisting of tight channels and pockets. It consists of four crystallographically independent zinc ions, each in a tetrahedral environment defined by four nitrogen atoms of four different ligands. This work was also corroborated by *in situ* NMR studies. The solid-state 13C NMR spectrum of kat-Zn(Melm)$_2$ indicates four symmetrically non-equivalent Melm-ligands. Samples of dia-Zn(MeIm)$_2$ are non-porous, exhibiting an almost completely flat nitrogen sorption curve.

4.4.1.4 Reversible Gas Sorption Driven by Temperature Baek et al. (2015) [59] used combined *in situ* single-crystal and synchrotron powder X-ray diffraction to determine reversible CO_2 sorption processes in a self-assembled and apparently non-porous organic crystal, 1,3,5-tris-(4-carboxyphenyl) benzene (H_3BTB) (Figure 4.20a). The host material is formed by a hydrogen bond network between H_3BTB and *N,N*-dimethylformamide (DMF) and by the π–π stacking between the H_3BTB moieties (Figure 4.20b). The material can be viewed as well-ordered array of cages which are tight-packed so that the cages are inaccessible from outside. The hydrogen bonds and π–π stacking are strong enough to give relatively high thermal stability up to ≈373 K at 1 bar. The DMF-forming cages could be flexible, providing transient pathways for guest diffusion. The encapsulated DMF molecules are disordered around a site of a threefold rotary inversion symmetry. These molecules can be completely removed in vacuum at 323 K, resulting in very stable crystal (Figure 4.20c). The unit cell volume decreased by 3.23% after removal of DMF molecules. Each cage has about 83 Å which is large enough for capturing small gas molecules such as CO_2.

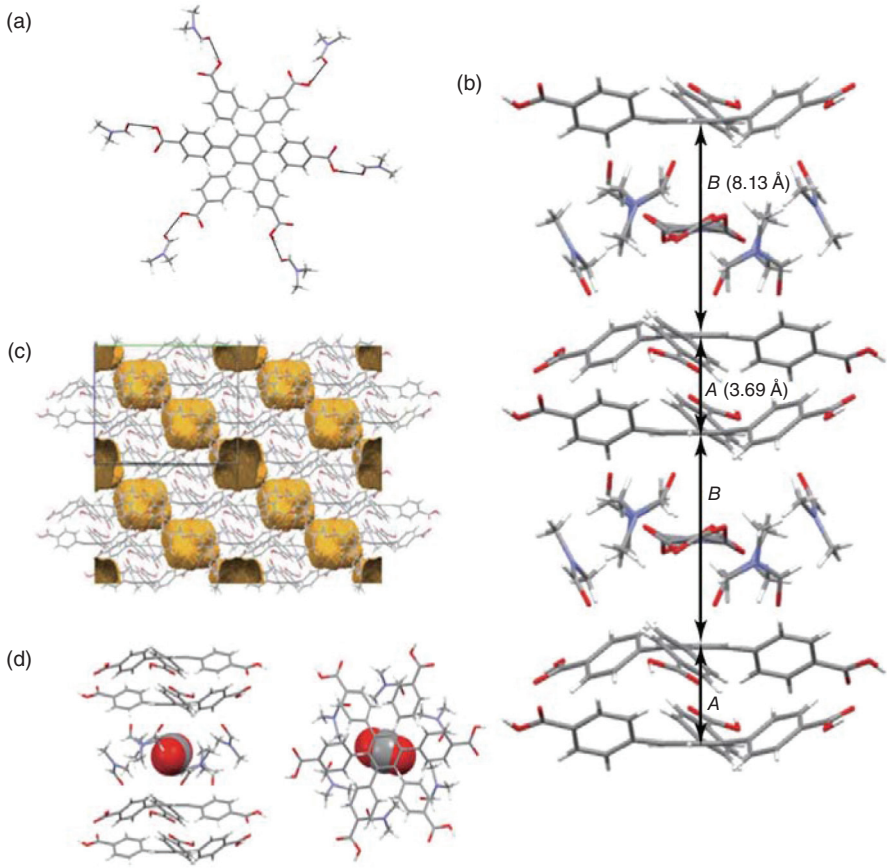

Figure 4.20 (a) Structure of (H_3BTB +DMF) showing the hydrogen bonding network. (b) Packing of (H_3BTB +DMF) moieties. Red color represents "O." (c) Structure after DMF molecules have been evacuated, showing the cages. (d) Views of the cage with a CO_2 molecule ($H_3BTB{\cdot}CO_2$). The CO_2 molecule is disordered around a site of a threefold rotary inversion symmetry and is depicted by a space-filling model. *Source*: Baek et al. 2015 [59]. Reproduced with permission of PNAS.

In situ single-crystal X-ray diffraction experiments were done under varying pressures at 323 K. It was found that even though there are no permanent channels connecting the isolated cages, all cages are filled at 25 bar of CO_2 pressure. One cage contains one CO_2 molecule and the cage is composed of two H_3BTB and six DMF molecules, with stoichiometry $(H_3BTB)_2(DMF)_6(CO_2)$. Therefore, the empty cages are permeable to CO_2 at high temperatures due to thermally activated transient pathways (molecular gating) between the cages. Figure 4.20d shows the cage

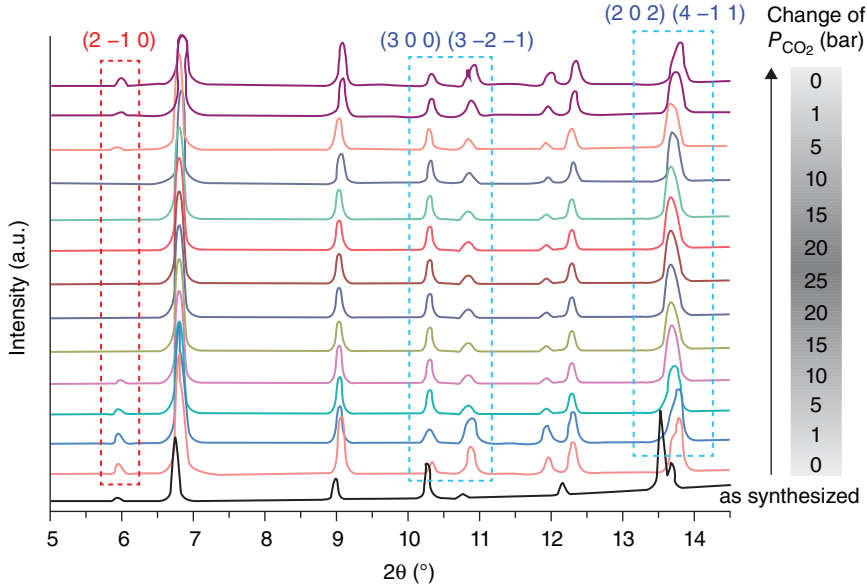

Figure 4.21 *In situ* synchrotron PXRD patterns under varying pressures of CO_2 at 323 K. The red dotted square represents the changes in diffraction peaks at the (2 –1 0) plane accompanying CO_2 adsorption and desorption. The blue dotted square represent the intensity changes in diffraction peaks accompanying framework expansions and contractions upon reversible CO_2 sorption. *Source*: Baek et al. 2015 [59]. Reproduced with permission of PNAS.

of (H_3BTB) with a CO_2 molecule. The disordered CO_2 molecule is depicted by a space-filling model.

Further variable-temperature *in situ* synchrotron powder X-ray diffraction studies also confirmed that the CO_2 sorption is reversible and driven by temperature increase (Figure 4.21). With combined solid-state NMR, they were also able to study the dynamical motion of CO_2.

4.4.1.5 Framework Formation in Action In order to understand the details of the complex crystallization process of lithium tartrate MOF, Yeung et al. [60] employed high-energy *in situ* synchrotron X-ray powder diffraction at the Diamond Light Source Beamline I12 to study the crystallizations and the metastable intermediates in the phase formation of a lithium tartrate MOF, Li_2(*meso*-$C_6H_6O_6$). Li_2(*meso*-$C_6H_6O_6$) has a monodentate binding site. They observed the successive crystallization and dissolution of three competing MOF phases in one reaction. As shown in Figure 4.22, which gives the three possible products, namely, the low-density phases **1** (Li_2(meso-$C_6H_4O_6$)$(H_2O)_{0.5}$, a metastable intermediate

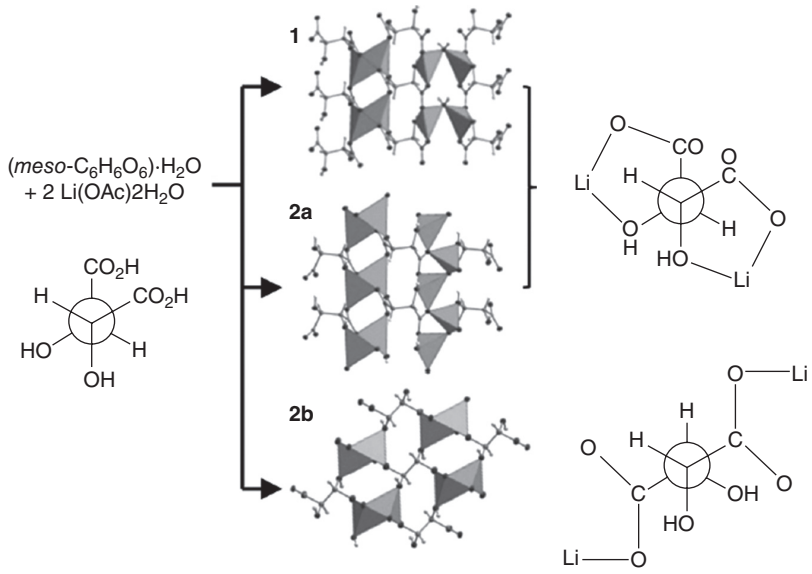

Figure 4.22 Three possible products in the formation of lithium meso-tartrates, showing ligand conformations and major binding modes. *Source*: Yueng et al. 2016 [60]. Reproduced with permission of John Wiley & Sons.

2a (Li_2(meso-$C_6H_4O_6$)(H_2O) (with gauche ligand conformation which is the preferred conformation of the mesotartaric acid), and **2b**, a denser Li_2(meso-$C_6H_4O_6$) phase, which has a monodentate binding feature. *In situ* X-ray diffraction confirmed compound **2b** to be the final thermodynamically stable product (Figure 4.23). They further determined the extent of crystallization as a function of reaction time, and quantified the reaction energy by determining the reaction rate constants and activation energies. The structure relationships between reactants and products were used to interpret different reaction rates (i.e., larger changes in conformation gave rise to higher activation energy).

4.4.1.6 Resin-Assisted Solvothermal MOF Synthesis

The [Co(NDC)(DMF)] (NDC = 2,6-naphthalenedicarboxylate) system is a system which is known to produce at least three distinct frameworks during the synthesis process. In order to determine the structural diversity observed in coordination polymers formed using Co(II) NDC and DMF, the system was probed by Moorhouse et al. [61] to determine, in particular, the factors influencing the preferential formation of one structure over another. The process involved the use of cation-impregnated polymer resin as both template and metal source in a relatively new technique in MOF synthesis.

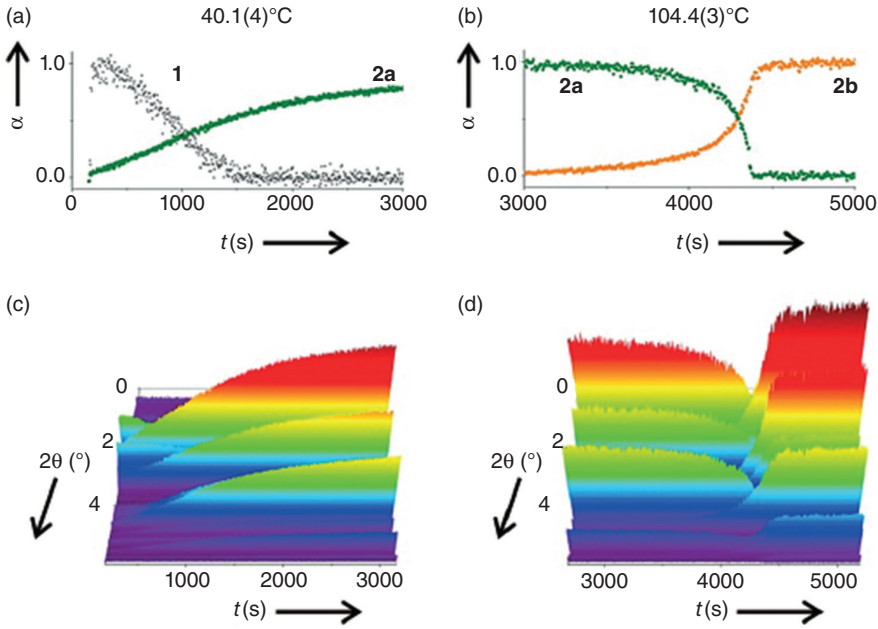

Figure 4.23 Solvothermal conversions between lithium tartrate MOFs, showing (a, b) the extent of crystallization as a function of reaction time (*t*). (c, d) *In situ* XRD data, where 2θ is the diffraction angle. (a, c) Hydrated phase **1** (gray points) is converted into metastable phase **2a** (green points), followed by (b, d) conversion of **2a** into the thermodynamic product **2b** (orange points). λ = 0.2326 Å. *Source*: Yueng et al. 2016 [60]. Reproduced with permission of John Wiley & Sons.

Reactions were conducted using angular-disperse XRD at Beamline I12, Diamond Light Source (with the Oxford-Diamond *In Situ* Cell (ODISC)). Further *in situ* energy-disperse XRD experiments were performed by using HASYLAB Beamline F3 of the DORIS synchrotron at the Hamburg campus. It was found that the resin-assisted synthesis resulted in the preferential formation of a topology previously impossible to synthesis in bulk form. The [Co(NDC)(DMF)] framework viewed along the *z*-axis (showing the diamond shape channels and coordinated DMF) is shown in Figure 4.24. The stack plot in Figure 4.25 shows *in situ* energy-dispersive XRD data obtained during the solvothermal formation of [Co(NDC)(DMF)] at 200°C. Reflections consistent with undissolved H_2NDC are observed initially at 2θ = 2.48° and 3.64°, then diminished and finally disappeared before the autoclave reaches 200°C. All reflections consistent with the [Co(NDC)(DMF)] phase appear concurrently. The framework MOF was formed as a pure phase which is monoclinic with a space group *C*2/*c* (*a* = 23.436(3) Å, *b* = 8.7733(6) Å, *c* = 7.219(1) Å, β = 97.80(2)°).

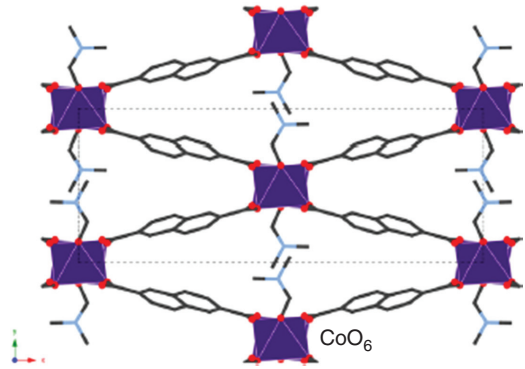

Figure 4.24 Structure of [Co(NDC)(DMF)] viewed along the *c*-axis showing coordinated DMF. Octahedral coordination spheres are shown as polyhedral. *Source*: Moorhouse et al. 2015 [61]. Reproduced with permission of Elsevier.

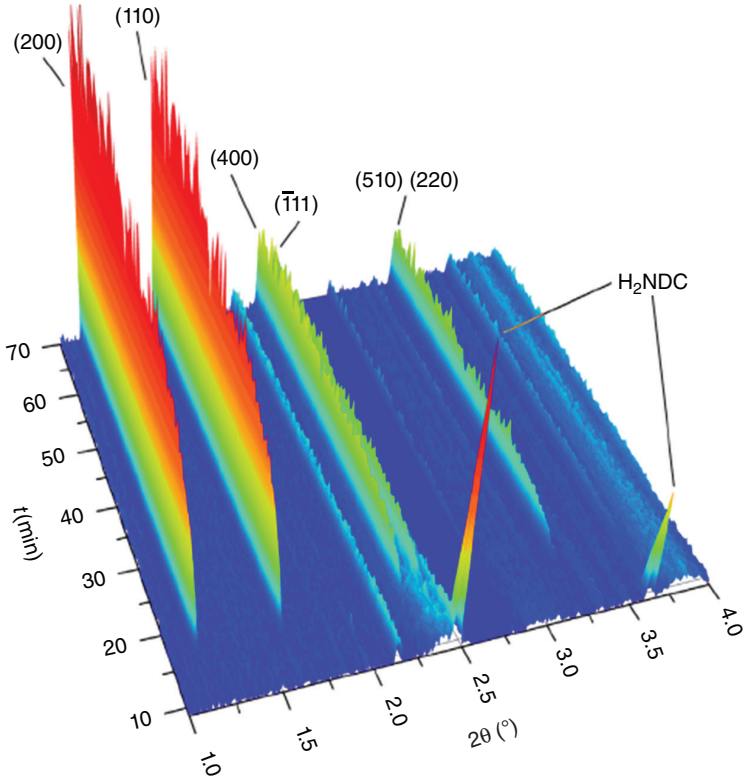

Figure 4.25 Three-dimensional-stack plot showing *in situ* angular-dispersive XRD data at 200°C. *Source*: Moorhouse et al. 2015 [61]. Reproduced with permission of Elsevier.

4.4.2 Laboratory X-ray Diffraction Studies

4.4.2.1 Location of Adsorbed CO_2 Molecules The highly porous compound HKUST-1 [62, 33] is composed of dimeric cupric tetracarboxylate units. HKUST-1 has a three-dimensional channel structure connecting a system of cages. The square-shaped pores are about 10 Å diameter, and the largest ones are hexagonal pores of about 18 Å in diameter. Using neutron diffraction, Wu et al. found that the unsaturated open Cu site plays an important role in enhancing binding of CO_2 molecules [32].

In Figure 4.26a, *in situ* experiments with CO_2 delivered at different partial pressures were conducted by Wong-Ng et al. [62] with a Panalytical X-ray diffractometer using the Anton Paar environmental chambers XRK 900 (gas flow conditions) under a series of CO_2 partial pressures (0.2, 0.4, 0.8, 1, and 6 bar). Several features of the X-ray patterns that are sensitive to occupancy of the cages by guest species were found. The X-ray patterns containing 311 and 222 reflections were shown: (1) refers to the as-received sample, (2) is the one that received treatment for 24 h at 150°C under flowing He, and exposure to mixture of CO_2/He with increasing fractions. The 311 intensity increases from near zero for hydrated sample 1 to dehydrated 2, then decreases back to small value as p_{CO_2} decreases, suggesting the empty pores become occupied by CO_2. Figure 4.26b gives an asymmetric unit structure.

One can identify two principal adsorption sites: at "open space" A-site near Cu, and around the B-site, the "octahedral site." Highly disordered CO_2 molecules were found. Using first principles calculations, Zhou et al. [76] predicted CO_2 to be linear with the Cu–O1–C angle of 110° (Figures 4.26c and 4.26d). The large open space in the vicinity enables the rotation of the CO_2 molecules. The CO_2 molecules in the octahedral cage are also disordered. It gives a single quadruple split site at the center of the cage (1/4, 1/4, 1/4) and four overlapped oxygen sites (unresolved double split) along the <111> directions. A plot of the occupancy of the "open space" site and the "octahedral cages" shows progressive increase as p_{CO_2} increases (Figure 4.26e). The open-space site is occupied preferentially. In summary, the adsorption is mainly on two sites, one is on top of the open Cu atom and another one is in the window opening of an octahedral cage. The metal–CO_2 binding is due to enhanced electrostatic interaction, and the framework CO_2 interaction is of the van der Waals type. The highly disordered CO_2 molecules result from the flowing versus static gas situation.

4.4.2.2 Materials Screening for Post-Combustion CO_2 Capture (In Situ XRD/DSC) Combined use of *in situ* X-ray diffraction and simultaneous differential scanning calorimetry (DSC) is a promising technique for rapid evaluation of the suitability of microporous materials for post-combustion CO_2 capture in both dry and wet conditions (particularly in the presence of water vapor which is a major component of post-combustion CO_2 capture). Using calorimetry, the enthalpy of adsorption for a gas can be directly measured at experimental conditions. This is especially advantageous in the situations of phase transitions, or gate-opening in the presence

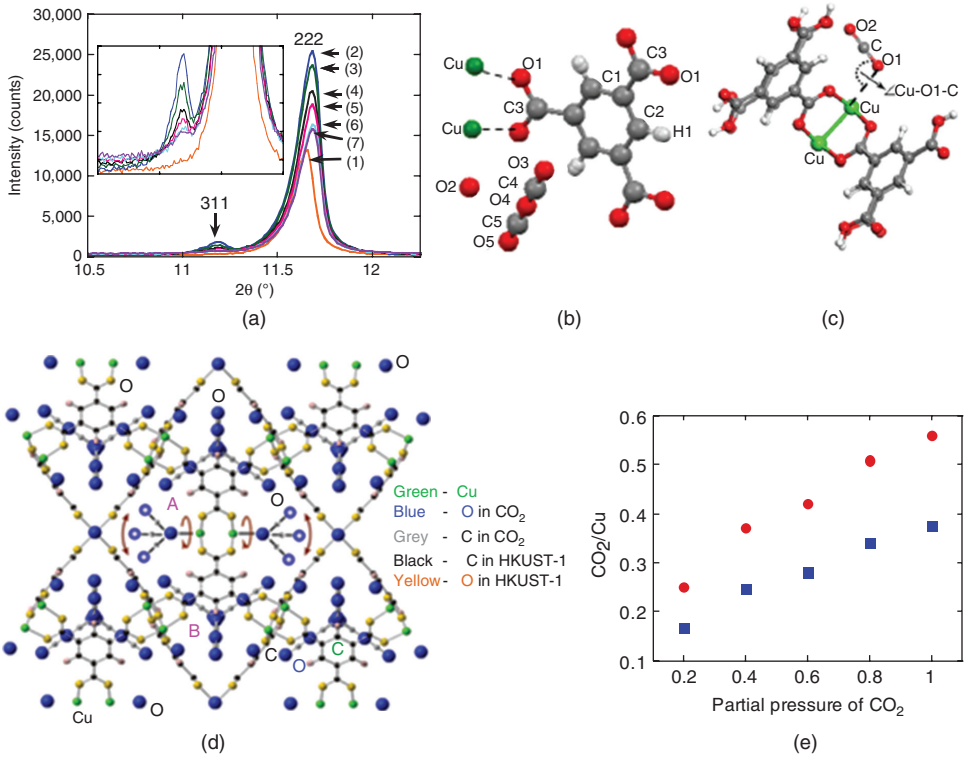

Figure 4.26 (a) *In situ* X-ray diffraction patterns under gas flow conditions under a series of partial pressures, from 0.2, 0.4, 0.8, 1 bar and higher, (1) as-received sample and (2) evacuated at 150°C under He for 24 h; (b) Atomic labeling scheme, including the disordered CO_2 molecules; (c) The structure of CO_2 molecule adsorption on the open Cu sites of HKUST-1; (d) A projection of the unit cell along ⟨110⟩ direction. Rotational disorder proposed for the CO_2 molecules located next to the Cu ions is illustrated by showing multiple molecule positions and further emphasized using arc arrows; (e) The occupancy of the "open space" site (round dots) and the "octahedral cages" (squares) increase progressively as p_{CO_2} increases [numbers in (a); colors in (e)]. *Source*: Wong-Ng et al. 2016. Reproduced with permission of Elsevier.

of guests. Woerner et al. [45] used this combined technique to study the performance and structural effect of CO_2 adsorption under static or dynamically varying humidity, temperature, and gas on a class of potential materials for CO_2 capture.

One example illustrating the applications of the simultaneous XRD-DSC technique is the open-framework compound ZIF-7, $Zn(bIm)_2$ (where bIm = 2-benzimidazolate). ZIF-7 is formed by connecting Zn metal clusters through the benzimidazole (BIM) linkers. It has a sodalite topology with a crystallographic six-membered ring pore opening (Figures 4.27a and 4.27b). The position of the benzene rings in the

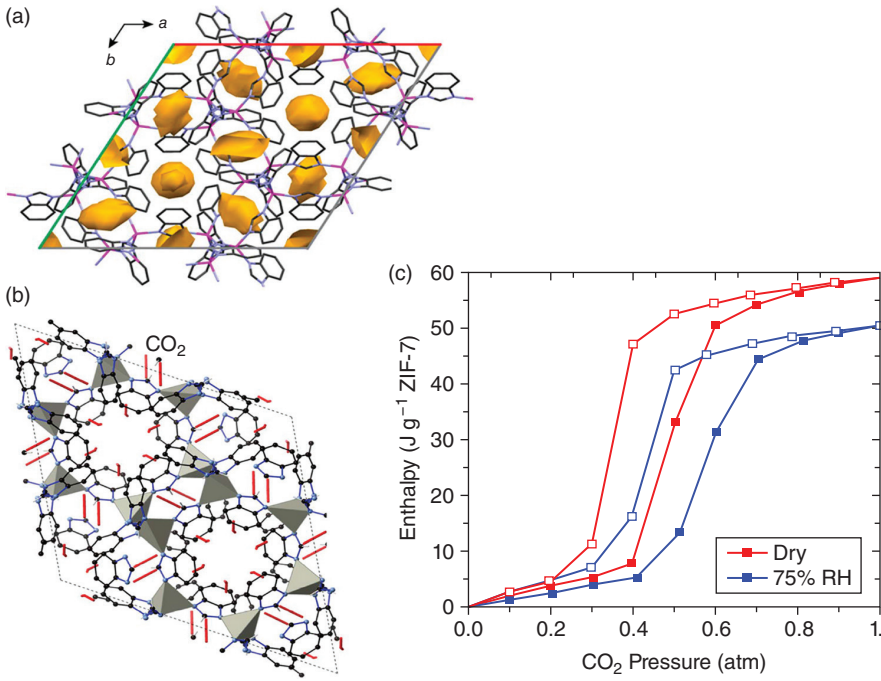

Figure 4.27 (a) Pore morphologies and accessible volumes (indicated by yellow surfaces) of ZIF-7; (b) structure of ZIF-7 (gate open) at 1 atm of CO_2. Zinc tetrahedra are shown in gray tone nitrogen in blue, carbon in black, and CO_2 in red. The CO_2 molecules are coordinated to the benzimidazolate rings; (c) Cumulative measured enthalpy isotherm of ZIF-7 during CO_2 adsorption–desorption with the XRD-DSC under dry (red) and 75% RH (blue) conditions. Closed symbols are from enthalpy measurements during adsorption, and open symbols are from desorption enthalpy measurements. *Source*: Woerner et al. 2015 [45]. Reproduced with permission of American Chemical Society.

optimized structure in vacuum narrows the pore entrance to ≈0.3 nm. However, the linkers have some freedom to rotate over a certain angle, allowing molecules larger than 0.3 nm to enter the main cavities.

In Figure 4.27c, cumulative enthalpy isotherms during CO_2 adsorption–desorption with XRD-DSC under dry (red) and 75% RH (blue) conditions are shown. The presence of water vapor thus reduces the measured enthalpy and therefore the capacity of ZIF-7 (85.2% of dry). Figure 4.27c shows the results of vacuum-humid atmosphere swings. However, relative to other studied sorbents [45], ZIF-7 still shows strong CO_2 affinity even in the presence of 75% RH. Successive XRD patterns under vacuum and under 75% RH CO_2 vacuum-humid 1 atm CO_2 swings are shown in Figure 4.28. As a summary, ZIF-7 appears to be ideally suited for post-combustion flue gas CO_2 capture.

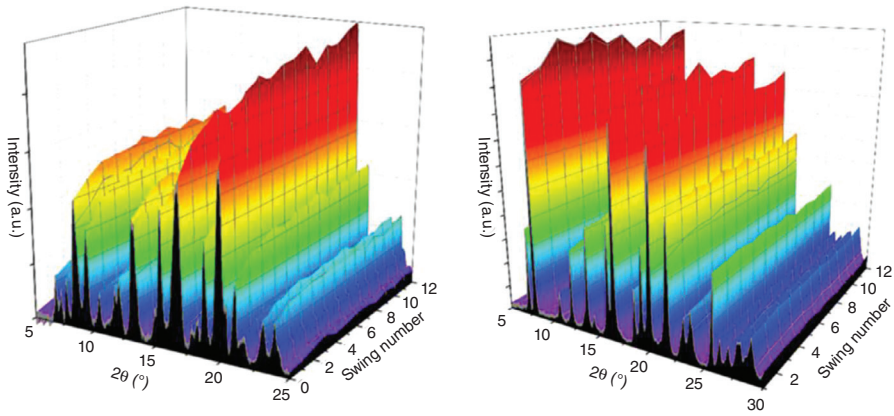

Figure 4.28 (a) Successive XRD patterns of ZIF-7 under vacuum and (b) under 75% RH CO_2 during vacuum. *Source*: Woerner et al. 2015 [45]. Reproduced with permission of American Chemical Society.

4.5 CONCLUSION

In situ diffraction techniques have been shown to be effective means for study of interactions of MOF with adsorbed guest molecules. In this chapter, we illustrated these techniques with seven examples, representing the capability of *in situ* diffraction for study of a gas adsorption mechanism, breathing of flexible MOFs, guest exchange studies, a guest-induced structural transition, a reversible transformation, probing of adsorption sites and binding sites of CO_2 and other gases, and *in situ* synthesis and phase formation of MOFs. In addition, the *in situ* diffraction techniques can also uniquely be used for monitoring a mechanochemical reaction-metastable intermediate, to capture metastable intermediates in successive crystallizations during the formation of an MOF, and to perform a snapshot analysis of transient molecular adsorption. Some of the studies used *in situ* diffraction combined with other techniques such as *in situ* NMR, and *in situ* DSC. As new *in situ* technology continues to evolve, we will be able to further our understanding of adsorption mechanisms, to facilitate the improvement of adsorption capability and the design of new applications.

REFERENCES

1. Etheridge, D.M.; Steele, L.P.; Langenfelds, R.L.; Francey, R.J.; Barnola, J.M.; Morgan, V.I. Natural and anthropogenic changes in atmospheric CO_2 over the last 1000 years from air in Antarctic ice and firn. *J. Geophys. Res. Atmos.* **1996**, *101*, 4115–4128.

2. Gammon, R.H.; Sundquist, E.T.; Fraser, P.J. History of carbon dioxide in the atmosphere. In *Atmospheric Carbon Dioxide and the Global Carbon Cycle*; DOE/ER-239; Trabalka, J.R., Ed.; U.S. Department of Energy: Washington, DC, **1985**; pp 25–62.
3. Espinal, L.; Poster, D.L.; Wong-Ng, W; Allen, A.J.; Green, M.L. Standards, data, and metrology needs for CO_2 capture materials—a critical review. *Environ. Sci. Technol.* **2009**, *47*, 11960–11975.
4. Choi, S.; Drese, J.; Jones, C.W. Absorbent materials for carbon dioxide capture from large anthropogenic point source. *ChemSusChem*. **2009**, *2*, 796–854.
5. Wang, B.; Cote, A.P.; Furukawa, H.; O'Keeffe, M.J.; Yaghi, O.M. Colossal cages in zeolite imidazolate frameworks as selective carbon dioxide reservoirs. *Nature* **2008**, *453*, 207.
6. Wong-Ng, W.; Kaduk, J.A.; Huang, Q.; Espinal, L.; Li, L.; Burress, J.W. Investigation of NaY zeolite with adsorbed CO_2 by neutron powder diffraction. *Micropor. Mesopor. Mater*. **2013**, *172*, 95–104.
7. Siriwardane, R.V.; Shen, M.-S.; Fisher, E.P.; Poston, J.A. Adsorption of CO_2 on molecular sieves and activated carbon. *Energy Fules* **2001**, *15*, 279–284.
8. Fripiat, J.J.; Cruz, M.M.; Bohor, B.F.; Thomas, J. Jr. Interlamellar adsorption of carbon dioxide by smectites. *Clays Clay Miner.* **1974**, *22*, 23–30.
9. Sayyah, I.; Lu, Y.; Mall, R.I.; Suslick, K.S. Mechanical activation of CaO-based adsorbates for CO_2 capture. *ChemSusChem.* **2013**, *6*, 193–198.
10. Ochoa-Fernández, E.; Rønning, M.; Grande, T.; Chen, D. Synthesis and CO_2 capture properties of nanocrystalline lithium zirconate. *Chem. Mater.* **2006**, *18*, 6037–6046.
11. Hutson, N.D. Structural effects on the high temperature adsorption of CO_2 on a synthetic hydrotalcite. *Chem. Mater.* **2004**, *16*, 4135–4143.
12. Zhou, H.C.; Kitagawa, S. Metal–organic frameworks (MOFs). *Chem. Soc. Rev.* **2014**, *43*, 5415–5418.
13. Dey, C; Kundu, T; Biswal, B.P.; Mallick, A.; Banerjee, R. Crystalline metal–organic frameworks (MOFs): synthesis, structure and function. *Acta Cryst.* **2014**, *B70*, 3–10.
14. Kitagawa, S.; Masuda, R. Chemistry of coordination space of porous coordination polymers. *Coord. Chem. Rev.* **2007**, *251*, 2490–2509.
15. Liu, Y; Wang, Z.U.; Zhou, H.-C. Recent advances in carbon dioxide capture with metal–organic frameworks. *Greenh. Gas Sci. Technol.* **2012**, *2*, 239–259.
16. Yaghi, O.M.; Li, Q. Reticular chemistry and metal–organic frameworks for clean energy. *MRS Bull.* **2009**, *34*, 682–690.
17. Morris, R.E.; Wheatley, P.S. Gas storage in nanoporous materials. *Angew. Chem., Int. Ed.* **2008**, *47*, 4966–4981.
18. Rowsell, J.L.C.; Yaghi, O.M. Metal–organic frameworks: a new class of porous materials. *Micropor. Mesopor. Mater.* **2004**, *73*, 3–14.
19. Wong-Ng, W.; Culp, J.T.; Chen, Y.-S.; Deschamps, J.; Marti, A. Flexible metal organic framework $\{[Ni(DpBz)][Ni(CN)_4]\}_n$, (DpBz = 1,4-bis(4-pyridyl)benzene) with an unusual Ni–N bond. *Solid State Sci.* **2016**, *52*, 1–9.
20. Wang, Q.M.; Shen, D.; Bülow, M.; Lau, M.L.; Deng, S.; Fitch, F.R.; Lemcoff, N.O.; Semanscin, J. Metallo-organic molecular sieve for gas separation and purification. *Micropor. Mesopor. Mater.* **2002**, *55*, 217–230.
21. Kitagawa, S.; Uemura, K. Dynamic porous properties of coordination polymers inspired by hydrogen bonds. *Chem. Soc. Rev.* **2005**, *34*, 109–119.

22. Furukawa, H.; Cordova, K.E.; O'Keeffe, M; Yaghi, O.M. The chemistry and applications of metal–organic frameworks *Science* **2013**, *341*, 1230444.
23. Gao, W.-Y.; Chrzanowski, M.; Ma, S. Metal-metalloporphyrin frameworks: resurging class of functional materials. *Chem. Soc. Rev.* **2014**, *43*, 5841–5866.
24. Li, B.; Zhang, Y.; Ma, D.; Ma, T.; Shi, Z.; Ma, S. Metal cation directed *de novo* assembly of a functionalized guest molecule into the nanospace of a metal–organic framework. *J. Am. Chem. Soc.* **2014**, *136*, 1202–1205.
25. Kauffman, K.L.; Culp, J.T.; Allen, A.J.; Espinal-Thielen, L.; Wong-Ng, W.; Brown, T.D.; Goodman, A.; Bernardo, M.P.; Pancoast, R.J.; Chirdon, D. Selective adsorption of CO_2 from light gas mixture by using a structurally dynamic porous coordination polymer. *Angew Chem. Int. Ed.* **2011**, *50*, 10888–10892.
26. Tranchemontagne, D.J.; Hunt, J.R.; Yaghi, O.M. Room temperature synthesis of metal–organic framework: MOF-5, MOF-74, MOF-177, MOF-199, and IRMOF-0. *Tetrahedron* **2008**, *64*, 8553–8557.
27. Culp, J.T.; Madden, C.; Kauffman, K.; Shi, F.; Matranga, C. Screening Hofmann compounds as CO_2 sorbents: nontraditional synthetic route to over 40 different pore-functionalized and flexible pillard cyanonickelates. *Inorg. Chem.* **2013**, *52*, 4205–4216.
28. Feng, D.; Wang, K.; Su, J.; Liu, T.-F.; Park, J.; Wei, Z.; Bosch, M.; Yakovenko, A.; Zou, X.; Zhou, H.-C. A highly stable zeotype mesoporous zirconium metal–organic framework with ultralarge pores. *Angew. Chem., Int. Ed.* **2014**, *54*, 149–54.
29. Culp, J.T.; Smith, M.R.; Bittner, E.; Bockrath, B. Hysteresis in the physisorption of CO_2 and N2 in a flexible pillard layer nickel cyanide. *J. Am. Chem. Soc.* **2008**, *130*, 12427–12434.
30. Bloch, E.D.; Hudson, M.R.; Mason, J.A.; Queen, W.L.; Zadrozny, J.M.; Chavan, S.; Bordiga, S.; Brown, C.M.; Long, J.R. Reversible CO binding enables tunable CO/H2 and CO/N2 separations in metal–organic frameworks with exposed divalent metal cations. *J. Am. Chem. Soc.* **2014**, *136*, 10752–10761.
31. Caskey, S.R.; Wong-Foy, A.G.; Matzger, A.J. Dramatic tuning of carbon dioxide uptake via metal substitution in a coordination polymer with cylindrical pores. *J. Am. Chem. Soc.* **2008**, *130*, 10870–10871.
32. Wu, H.; Simmons, J.M.; Srinivas, G.; Zhou, W.; Yildirim, T. Adsorption sites and binding nature of CO_2 in prototypical metal–organic frameworks-A combined neutron diffraction and first-principles study. *J. Phys. Chem. Lett.* **2010**, *1*, 1946–1951.
33. Chui, S.S.-Y.; Lo, S.M.-F.; Charmant, J.P.H.; Orpen, A.G.; Williams, I.D. A chemically functionalizable nanoporous material $[Cu_3(TMA)_2(H_2O)_3]_n$. *Science* **1999**, *283*, 1148–1150.
34. Wong-Ng, W.; Kaduk, J.A.; Siderius, D.L.; Allen, A.L.; Espinal, L. Boyerinas, B.M.; Levin, I.; Suchomel, M.R.; Ilavsky, J.; Li, L. Reference diffraction patterns, microstructure, and pore size distribution for the copper (II) benzene-1,3,5-tricarboxylate metal organic framework (Cu-BTC) compounds. *Powd. Diffr.* **2015**, *30*, 2–13.
35. Zhang, J.-P, Liao, P.-Q., Zhou, H.-L., Lin, R.-B., Chen, X.-M. Single crystal X-ray diffraction studies on structural transformations of porous coordination polymers. *Chem. Soc. Rev.* **2014**, *43*, 5789–5814.
36. Espinal, L.; Wong-Ng, W.; Kaduk, J.A.; Allen, A.J.; Snyder, C.R.; Chiu, C.; Siderius, D.W.; Li, L.; Cockayne, E.; Espinal, A.E. Time dependent CO_2 sorption hysteresis in a one-dimensional microporous octahedral molecular sieve, *J. Am. Chem. Soc.* **2012**, *134*, 7944–7951.

37. Allen, A.J.; Espinal, L.; Wong-Ng, W.; Queen, W.L., Brown, C.M.; Kline, S.R.; Kauffman, K.L.; Culp, J.T.; Matranga, C. In situ structural dynamics of flexible metal–organic frameworks for selective CO_2 adsorption. *J. Alloys Compd.* **2015**, *647*, 24–34.
38. Wong-Ng, W.; Culp, J.T.; Chen, Y.S.; Zavalij, P.; Espinal, L.; Siderius, D.W.; Allen, A.J.; Scheins, S.; Matranga, C. Improved synthesis and crystal structure of the flexible pillared layer porous coordination polymer: Ni(1,2-bis(4-pyridyl)ethylene)[$Ni(CN)_4$]. *CryEngComm* **2013**, *15*, 4684–4693.
39. Wong-Ng, W.; Kaduk, J.A.; Espinal, L.; Suchomel, M; Allen, A.J.; Wu, H. High-resolution synchrotron x-ray diffraction study of bis(2-methylimidazolyl)-zinc, $C_8H_{10}N_4Zn$ (ZIF-8). *Powd. Diffr.* **2011**, *26*, 234–237.
40. Wong-Ng, W.; Kaduk, J.A.; Wu, H.; Suchomel, M. Synchrotron x-ray studies of metal–organic framework M_2(2,5-dihydroxyterephthalte), M = (Mn, Co, Ni, Zn) (MOF74). *Powd. Diffr.* **2012**, *27*, 256–262.
41. Cox, J.M.; Walton, I.M.; Benson, C.A.; Chen, Y.-S.; Benedict, J.B. A versatile environmental control cell for in situ guest exchange single-crystal diffraction. *J. Appl. Cryst.* **2015**, *48*, 578–581.
42. Warren, J.E.; Pritchard, R.G.; Abram, D.; Davies, H.M.; Savarese, T.L.; Cash, R.J.; Raithby, P.R.; Morris, R.; Jones, R.H.; Teat, S.J. A prototype environmental gas cell for in situ small-molecule X-ray diffraction. *J. Appl. Cryst.* **2009**, *42*, 457–460.
43. Cernik, R.J.; Clegg, W.; Catlow, C.R.A.; Bushnell-Wye, G.; Flaherty, J.V.; Greaves. G.N.; Burrows, I.; Taylor, D.J.; Teat, S.J.; Hamichi, M. A new high-flux chemical and materials crystallography station at the SRS Daresbury. 1. Design, construction and test results. *J. Synchrotron Rad.* **1997**, *4*, 279–286.
44. Yufit, D.S.; Howard, J.A.K. Simple pressure cell for single-crystal X-ray crystallography. *J. Appl. Cryst.* **2005**, *38*, 583–586.
45. Woerner, W.R.; Plonka, A.M.; Chen, X.; Banerjee, D.; Thallapally, P.K.; Parise, J.B. Simultaneous in situ X-ray diffraction and calorimetric studies as a tool to evaluate gas adsorption in microporous materials. *J. Phys. Chem. C.* **2015**, *120*, 360–369.
46. Moorhouse S.J; Vranjes, N.; Jupe, A.; Drakopoulos, M.; O'Hare, D. The oxford-diamond in situ cell for studying chemical reactions using time-resolved x-ray diffraction. *Rev. Sci. Instrum.* **2012**, *83*, 084101. DOI: 10.1063/1.4746382.
47. Allan, P. K.; Xiao, B.; Teat, S. J.; Knight, J.W.; Morris, R.E. In situ single-crystal diffraction studies of the structural transition of metal–organic framework copper e-sulfoisophthalate, Cu-SIP-3. *J. Am. Chem. Soc.* **2010**, *132*, 3605–3611.
48. Takamizawa, S.; Nataka, E.-I; Akatsuka, T.; Miyake, R.; Kakizaki, Y.; Yakeuchi, H.; Maruta, G.; Takeda, S. Crystal transformation and host molecular motions in CO_2 adsorption process of a metal benzoate pyrazine (M^{II} = Rh, Cu). *J. Am. Chem. Soc.* **2010**, *132*, 3783–3792.
49. Takamizawa, S.; Nataka, E.; Akatsuka, T.; Miyake, R.; Kakizaki, Y.; Takeuchi, H.; Maruta, G.; Takeda, S. Crystal transformation and host molecular motions in CO_2 adsorption process of a metal benzoate pyrazine (MII) Rh, Cu). *J. Am. Chem. Soc.* **2010**, *132*, 3783–3792
50. Liao, P.-Q.; Zhou, D.-D.; Zhu, A.-X.; Jiang, L.; Lin, R.-B.; Zhang, J.-P., Chen, X.-M. Strong and dynamic CO_2 sorption in a flexible porous framework possessing guest chelating claws. *J. Am. Chem. Soc.* **2012**, *134*, 17380–17383.
51. Miller, S.R.; Wright, P.A.; Devic, T.; Serre, C.; Ferey, G.; Llewellyn, P.L.; Denoyel, R.; Gaberova, L.; Filinchuk, Y. Single crystal X-ray diffraction studies of carbon dioxide

and fuel-related gases adsorbed on the small pore scandium terephthalate metal organic framework, $Sc_2(O_2CC_6H_4CO_2)_3$. *Langmuir* **2009**, *25*, 3618–3626.
52. Alhamami, M.; Doan, H.; Cheng, C.-H. A review of breathing behaviors of metal-organic-frameworks (MOFs) for gas adsorption. *Materials.* **2014**, *7*, 3198–3250.
53. Seere, C.; Millange, F.; Thouvenot, C.; Nogues, M.; Marsolier, G.; Louër, D.; Férey, G. Very large breathing effect in the first nanoporous chromium (III)-based solids: MIL-53 or $Cr_{III}(OH)\cdot\{O_2C\text{-}C_6H_4\text{-}CO_2\}\cdot\{HO_2C\text{-}\ C_6H_4\text{-}\ CO_2H\}_x\cdot H_2O_y$. *J. Am. Chem. Soc.* **2002**, *124*, 13519–13526.
54. Seere, C.; Bourrelly, S.; Vimont, A.; Ramsahye, N.; Maurin, G.; Llewellyn, M.D.; Filinchuk, Y.; Leynaud, O. Barnes, P.; Férey, G. An explanation for te very large breathing effect of a metal–organic framework during CO_2 adsorption, *Adv. Mater.* **2007**, *19*, 2246–2251.
55. Llewellyn, P.L.; Maurin, G.; Devic, T.; Lorea-Serna, S.; Rosenbach, N.; Serre, C.; Bourrelly, S.; Horeajada, P.; Filinchuk, Y.; Ferey, G. Prediction of the conditions for breathing of metal organic framework materials using a combination of X-ray powder diffraction, microcalorimetry, and molecular simulation. *J. Am. Chem. Soc.* **2008**, *130*, 12808–12814.
56. Carrington, E.J.; Vitórica-Yrezábal, I.J.; Brammer, L. Crystallographic studies of gas sorption in metal–organic frameworks. *Acta Cryst.* **2014**, *B70*, 404–422.
57. Henke, S.; Wieland, D.C. F.; Mikhail, M.; Paulus, M.; Sternemann, C.; Yusenko, K.; Fisher, R.A. Multiple phase-transitions upon selective CO_2 adsorption in an alkyl ether functionalized metal–organic framework- an in situ diffraction study. *CrystEngComm* **2011**, *13*, 6399–6404.
58. Katsenis, A.D.; Puškarić, A.; Ŝtrukil1, V.; Mottillo, C.; Julien, P.A.; Užarevic, K.; Minh-Hao Pham, M.-H.; Do, T.-O.; Kimber, S.A.J. Predrag Lazić; Magdysyuk, O.; Dinnebier, R.E.; Halasz, I.; Friščić, T. In situ X-ray diffraction monitoring of a mechanochemical reaction reveals a unique topology metal–organic framework. *Nature Comm*. **2015**, DOI: 10.1038/ncomms7662
59. Baek, S.B.; Moon, D.; Graf, R.; Cho, W.J.; Park, S.W.; Yoon, T.-U.; Cho, S.J.; Hwang, I.-C; Bae, Y.-S.; Spiess, H.W.; Lee, H. C.; Kim, K.S. High-temperature in situ crystallographic observation of reversible gas sorption in impermeable organic cages. *PNAS* **2015**, *112* (46) 14156–14161.
60. Yueng, H.-M.; Wu, Y.; Henke, S.; Cheetham, A.K.; O'Hare, D.; Walton, R.I. In situ observation of successive crystallization and metastable intermediates in the formation of metal- organic frameworks. *Angew. Chem., Int.Ed.* **2016**, *55*, 2012–2016.
61. Moorhouse, S.J.; Wu, Y.; O'Hare, D. An in situ study of resin-assisted solvothermal metal- organic framework synthesis. *J. Solid State Chem.*, **2015**, *236*, p. 209–214.
62. Wong-Ng, W.; Levin, I.; Kaduk, J. A.; Espinal, L.; Wu, H. CO_2 capture and positional disorder in bis(135-benzenetricarboxylate) tri-copper hydrate: an in situ laboratory x-ray powder diffraction study, *J. Alloys Compd.* **2016**, *656*, 200–205.
63. Park, J.H.; Choi, K.M.; Jeon, H.J, Choi, Y.J.; Kang, J.K. In-situ observation for growth of hierarchical metal–organic frameworks and their self-sequestering mechanism for gas storage. *Sci. Rep.* **2015**, *5*: 12045 (1–8).
64. Yang, C.; Wang, X.; Omary, M.A. Crystallographic observation of dynamic gas adsorption sites and thermal expansion in a breathable fluorous metal–organic framework, *Angew. Chem., Int. Ed.* **2009**, *48*, 2500–2505.

65. Wu, Y.; Breeze, M.I.; Clarkson, G.J.; Millange, F.; O'Hare, M.; Walton, R.I. Exchange of coordinated solvent during crystallization of a metal–organic framework observed by in situ high-energy X-ray diffraction. *Angew. Chem.* **2016**, *55*, 4992–4996. DOI: 10.1002/anie.201600896
66. Schröder, M.; Alexander, J.B.; Yang, S. Gas-induced structural transitions in metal–organic frameworks. ESRF report for experiment CH3368 at beamline ID31, **2010**.
67. Liu, Y.; Wang, A.U.; Zhou, H.-C. Recent advances in carbon dioxide capture with metal–organic frameworks, *Greenhouse Gas Sci. Technol.* **2012**, *2*, 239–259.
68. Queen, W.L.; Hudson, M.R.; Bloch, E.D.; Mason, J.A.; Gonzalez, M.I.; Lee, J.S.; Gygi, D.; Howe, J.D.; Lee, K.; Daaaaaarwish, T.A.; James, M.; Peterson, V.K.; Teat, S.J.; Smit, B.; Neaton, J.B.; Long, J.R.; Brown, C.M. Comprehensive study of carbon dioxide adsorption in the metal–organic frameworks M_2(dobdc) (M = Mg, Mn, Fe, Co, Ni, Cu, Zn, *Chem. Sci.* **2014**, *5*, 4569–4581.
69. Halder, G.J.; Kepert, C.J. In situ single-crystal x-ray diffraction studies of desorption and sorption in a flexible nanoporous molecular framework material, *J. Am. Chem. Soc.* **2005**, *127*, 7891–7900.
70. Iqbal, N.; Wang, X.; Yu, J.; Jabeen, N.; Utlah, H.; Ding, B. In situ synthesis of carbon nanotube doped metal–organic frameworks for CO_2 capture. *RSC Adv.* **2016**, *6*, 4382–4386. (in situ MOF74 preparation), no diffraction.
71. Wu, Y.; Moorhouse, S.J.; O'Hare, D. Time-resolved in situ diffraction reveals a solid-state rearrangement during solvothermal MOF synthesis. *Chem. Mater.* **2015**, *27*(21), 7236–7239.
72. Millange, F.; Medina, M.I.; Guillou, N.; Férey, G.; Golden, K.M.; Walton, R.I. Time-resolved in situ diffraction study of the solvothermal crystallizaiton of some prototypical metal–organic frameworks. *Angew. Chem, Int. Ed.* **2010**, *49*, 763–766.
73. Van de Voorde, B.; Munn, A.S.; Guillou, N.; Millange, F.; De Vos, D.E.; Walton, R.I. Adsorption of N/S heterocycles in the flexible metal–organic framework MIL-53(FeIII) studied by in situ energy dispersive X-ray diffraction. *Phys. Chem. Chem. Phys.* **2013**, *15*, 8606–8615.
74. Kubota, R.; Tashiro, S.; Shiro, M.; Shionoya, M. In situ X-ray snapshot of transient molecular adsorption in a crystalline channel, *Nat. Chem.* **2014**, *6*, 913–918.
75. Jacobs, T.; Lloyd, G. O.; Gertenbach, J.-A.; Muller-Nedebock, K. K.; Esterhuysen, C.; Barbour, L.J. In situ X-ray structural studies of a flexible host responding to incremental gas loading. *Angew. Chem., Int. Ed.* **2012**, *51*, 4913–4916.
76. Zhou, C.; Cao, L.; Wei, S.; Zhang, Q.; Chen, L. A first principles study of gas adsorption, *Comput. Thero. Chem.* **2011**, *976*(1-3), 153–160.